JGR Planets

RESEARCH ARTICLE

10.1029/2025JE009352

Radiation Transport Through the Martian Atmosphere as a Function of the Zenith Angle

Salman Khaksari[1], **Phillip H. Phipps**[2,3,4], **Robert F. Wimmer-Schweingruber**[1], **Timothy J. Stubbs**[4], **Mark D. Looper**[5], **Jingnan Guo**[6,7], **Gabin Charpentier**[8,9,10], **Bent Ehresmann**[11], **Jan Leo Löwe**[1], **Daniel Matthiä**[12], **Donald M. Hassler**[11], **Cary Zeitlin**[13], **and Sven Löffler**[1]

[1]Institute of Experimental and Applied Physics, Christian-Albrechts-University, Kiel, Germany, [2]University of Maryland, Baltimore, MD, USA, [3]Center for Research and Exploration in Space Science and Technology (CRESST-II), Greenbelt, MD, USA, [4]NASA Goddard Space Flight Center, Greenbelt, MD, USA, [5]The Aerospace Corporation, Los Angeles, CA, USA, [6]Deep Space Exploration Laboratory/School of Earth and Space Sciences, University of Science and Technology of China, Hefei, PR China, [7]CAS Center for Excellence in Comparative Planetology, USTC, Hefei, PR China, [8]Centre National D'Études Spatiales (CNES), Toulouse, France, [9]TRAD Tests & Radiations, Labège, France, [10]ISAE-SUPAERO, Université de Toulouse, Toulouse, France, [11]Solar System Science & Exploration Division, Southwest Research Institute, Boulder, CO, USA, [12]German Aerospace Center (DLR), Institute of Aerospace Medicine, Cologne, Germany, [13]Leidos Corporation, Houston, TX, USA

Key Points:

- We model the flux of secondary particles on Mars as a function of the zenith angle of incoming primary protons
- Results enable the calculation of surface radiation fluxes from Galactic Cosmic Rays and Solar Energetic Particles by incorporating angle-dependent secondary particle fluxes
- Our model shows how atmospheric column depth varies with zenith angle, shaping radiation directionality and conditions at Gale Crater

Correspondence to:

S. Khaksari and P. H. Phipps,
khaksari@physik.uni-kiel.de;
phillip.h.phipps@nasa.gov

Citation:

Khaksari, S., Phipps, P. H., Wimmer-Schweingruber, R. F., Stubbs, T. J., Looper, M. D., Guo, J., et al. (2025). Radiation transport through the Martian atmosphere as a function of the zenith angle. *Journal of Geophysical Research: Planets*, *130*, e2025JE009352. https://doi.org/10.1029/2025JE009352

Received 1 AUG 2025
Accepted 30 NOV 2025

Author Contributions:

Conceptualization: Robert F. Wimmer-Schweingruber, Timothy J. Stubbs
Data curation: Jan Leo Löwe
Methodology: Salman Khaksari, Phillip H. Phipps, Robert F. Wimmer-Schweingruber, Mark D. Looper, Jingnan Guo
Supervision: Robert F. Wimmer-Schweingruber, Timothy J. Stubbs
Validation: Salman Khaksari, Phillip H. Phipps, Mark D. Looper, Gabin Charpentier, Daniel Matthiä
Writing – review & editing: Salman Khaksari, Phillip H. Phipps, Mark D. Looper, Jingnan Guo, Gabin Charpentier, Jan Leo Löwe, Daniel Matthiä

Abstract The topographic influence of the radiation environment on the Martian surface radiation is crucial for future human exploration. Topographic maps help assess radiation flux variations, aiding in hazard evaluation. Creating a global radiation map requires accounting for seasonally varying atmospheric density, heliospheric modulation, and topography. Here, we use a radiation model to derive the flux of secondary downward particles generated by the interaction of primary protons with the Martian atmosphere. Our model examines two key factors: (a) the dependence of atmospheric column depth on the zenith angle, affecting radiation directionality as horizon-arriving particles traverse more atmosphere than vertical ones and (b) atmospheric conditions at surface heights in Gale Crater, crucial for developing radiation dose maps that incorporate topographic effects. Our model is validated against Radiation Assessment Detector measurements and benchmarked with existing models. We construct response matrices representing the ratio of secondary particles at the Martian surface to primary inputs across zenith angles, assessing atmospheric effects. We combine these matrices with the incident spectrum to compute secondary particle fluxes from all zenith angles for Galactic Cosmic Rays and Solar Energetic Particles. These fluxes will be integrated into a topographic map of Mars in a follow-up study, providing a detailed representation of surface radiation levels across different terrains. This approach aids mission planners in identifying safe landing sites for astronauts.

Plain Language Summary Radiation on the surface of Mars is influenced by the planet's topography, which is an important factor for future human exploration. Understanding how radiation levels vary across different terrains can help identify safer landing sites for astronauts. To study this, we used a radiation model to calculate how high-energy protons from space interact with the Martian atmosphere, producing secondary particles that reach the surface. Our model focuses on two key aspects: (a) how the amount of atmosphere particles travel through, depends on the angle at which they enter the atmosphere, which affects radiation levels at different locations, and (b) how atmospheric conditions at different surface heights, such as in Gale Crater, impact radiation exposure. We validated our model using data from the Radiation Assessment Detector on the Curiosity rover and compared it with previous models. By analyzing how secondary particles form at different angles, we created a method to calculate radiation fluxes from Galactic Cosmic Rays and Solar Energetic Particles across the Martian surface. In future work, we will integrate these results into a topographic radiation map of Mars, which will help assess radiation risks in different regions and support mission planning for future astronauts.

1. Motivation and Introduction

Missions beyond low-Earth orbit, such as those to the Moon or Mars, expose astronauts to significantly higher cosmic radiation due to the loss of Earth's magnetic shielding present in low-Earth orbit. Deep space exploration entails exposure to two main sources of high-energy particle radiation: Galactic Cosmic Rays (GCRs) and Solar

Energetic Particles (SEPs). GCRs are characterized by their constant presence, mainly composed of protons and helium ions, accounting for approximately 87% and 12% of their overall composition, respectively (Guo, Zeitlin, et al., 2021; Simpson, 1983). GCRs also include trace amounts of heavier nuclei like carbon, nitrogen, oxygen, and iron (Simpson, 1983). In contrast, SEPs primarily consist of rapidly accelerated protons and electrons originating from sporadic solar eruptions. Subsequently, these highly energetic particles disperse throughout interplanetary space, adding complexity to the intricate radiation environment that astronauts face during missions beyond Earth's protective magnetosphere (Guo et al., 2024; Jun et al., 2024).

Space missions face challenges both during the cruise phase and while staying on Mars (Barcellos-Hoff et al., 2015; Cucinotta & Durante, 2006). SEPs and GCRs play critical roles in the context of space radiation exposure. The former can induce acute biological and technological effects due to their high fluxes during solar events, posing immediate hazards to astronauts (Kamiya et al., 2015). In contrast, GCRs, characterized by their higher energy and persistent presence, are of greater concern for long-term astronaut safety and radiation exposure on the Martian surface, especially given the limited shielding provided by the Martian atmosphere (Guo, Zeitlin, et al., 2021; Lobascio et al., 2018). Long-term exposure to GCRs can lead to serious health issues like cancer, cataracts, and nervous system damage (Cucinotta et al., 2014; Kennedy, 2014; Khaksarighiri et al., 2021).

After traversing the interplanetary expanse to Mars, GCRs undergo dynamic interactions with the Martian atmosphere. These interactions result in energy loss via ionization and the production of secondary particles through spallation and fragmentation.

The atmospheric cutoff energy for primary protons on Mars is approximately 160 MeV/nuc (Guo, Wimmer-Schweingruber, et al., 2019). This energy represents the minimum required for a proton to penetrate the Martian atmospheric column at Gale Crater, which has an average depth of about 21 g/cm^2 of CO_2. Protons with energies below this threshold are largely stopped by the atmosphere, and the resulting surface dose is primarily due to secondary particles—electrons, gamma rays, and neutrons—produced by interactions of these primary protons.

Given a requisite energy threshold, these particles can reach the Martian surface and penetrate into the subsurface strata, where their interaction with the soil generates albedo particles that also contribute to the radiation environment on the Martian surface. Consequently, the radiation environment extant on the Martian surface diverges notably from the conditions prevalent in deep space (Guo, Zeitlin, et al., 2021; Wilson et al., 2004).

In deep space, radiation is nearly isotropic, emanating uniformly from all directions across the full 4π steradian solid angle. However, when located on the Martian surface, the planet itself acts as a robust shield, against energetic particle radiation that would come from the bottom half of the full solid angle. The local topographical features can also play a crucial role in surface radiation (Ehresmann et al., 2021; Guo, Khaksarighiri, et al., 2021). Depending on the characteristics of these features, they can either enhance health risks to astronauts or provide potential shelter during their missions.

One key aspect of this radiation environment is the variation in the flux of radiation at the Martian surface regarding the zenith angle (Khaksarighiri et al., 2023; Wimmer-Schweingruber et al., 2015), with this variability closely related to changes in the column mass of the Martian atmosphere. The Martian atmosphere, although significantly thinner than Earth's, still exerts a notable influence on the radiation reaching the surface, especially for particles below a few GeV/nuc. As the incident angle of incoming particles changes with the zenith angle, so does the interaction between these particles and the Martian atmosphere. The modulation effect of Mars' atmosphere on the surface radiation has been shown to be present at both daily and seasonal time scales (Guo et al., 2015, 2017; Rafkin et al., 2014).

Obtaining precise insights into radiation flux variations with changing zenith angles is critical for establishing guidelines and protective measures to mitigate radiation exposure during surface operations. Understanding the intricate dynamics of radiation flux is important because of Mars' diverse topography and its effect on zenith angle variations, particularly in the context of missions spanning various regions. This understanding plays a crucial role in assessing Mars' habitability, as it allows us to refine our comprehension of how the Martian atmosphere influences radiation flux at varying zenith angles and identify promising areas for future exploration and colonization.

The Radiation Assessment Detector (RAD), onboard the Mars Science Laboratory's (MSL) Curiosity rover, has been monitoring the surface radiation on Mars for more than a decade since its landing in August 2012 (Hassler et al., 2012).

As MSL Curiosity rover traverses the Martian surface, its orientation in relation to the planet's topography fluctuates, leading to variations in its inclination. In a study by Wimmer-Schweingruber et al. (2015), these variations were used to investigate the shielding impact of the Martian atmosphere on radiation. The findings indicated that the radiation field exhibits nearly isotropic characteristics, with a slight increase in shielding observed at higher zenith angles. However, this study was constrained to rover tilt angles of $\lesssim 15°$. To gain a more comprehensive understanding of the radiation directionality across a broader zenith angle range (θ), we conducted a three-dimensional Monte Carlo simulation using GEANT4 (Khaksarighiri et al., 2023). This simulation allowed us to establish the dependence of surface dose rates on θ by modeling the interaction between incoming GCRs and the Martian atmosphere. The results from our model reveals that the surface radiation dose is non-isotropic on Mars, particularly at zenith angles exceeding 60°. While an isotropic behavior cannot be excluded at the 95% confidence level within the $\sim 25°$ inclination angle range experienced by Curiosity during its mission on Mars, this observation aligns with and extends the previous study by Wimmer-Schweingruber et al. (2015), which had a narrower coverage of inclination angles.

Additionally, a fraction of the radiation encountered on the Martian surface exhibits an upward trajectory. These secondary, upward-directed albedo particles originate as by-products of the interaction between GCRs and the Martian soil. Notably, Guo, Khaksarighiri, et al. (2021) estimated that albedo radiation, quantified in terms of the absorbed dose measured by RAD, accounts for approximately 19% of the total surface dose on flat terrain and slightly higher with surface structures such as buttes or mountains. In essence, this implies that the preponderance of the radiation detected on the Martian surface stems from downward-directed particles.

At a zenith angle of $\theta = 0°$, the atmospheric column depth is about ~ 21 g/cm^2 at Curiosity's location in Gale crater averaged over a Martian year (Gómez-Elvira et al., 2012). For comparison, at a zenith angle of $\sim 90°$ the corresponding column depth is as large as ~ 400 g/cm^2.

In this study, we seek to quantify the flux of secondary particles reaching the Martian surface, while investigating the role of the Martian atmosphere and topography in their production and transport. To achieve this, we employ a zenith angle-dependent model to construct a multidimensional look-up table, which will facilitate the estimation of radiation doses based on the flux of secondary particles. This table will incorporate critical parameters such as elevation angle, atmospheric pressure, and solar modulation, thereby enabling a comprehensive evaluation of radiation exposure under varying environmental conditions.

Our methodology involves generating flux spectra at the lower boundary of the Martian atmosphere, which will subsequently serve as inputs for radiation dose calculations. Here, we will focus on the impact of protons originating from GCRs and SEPs as they interact with the Martian atmosphere. This will allow us to assess the atmospheric influence on primary radiation, with a particular emphasis on how atmospheric conditions alter the incoming radiation flux.

In the following chapters, we begin by outlining the development of our Mars atmospheric model, describing how it was constructed and refined using Geant4. A central part of this model involves building matrices that represent the ratio of secondary particles reaching the Martian surface to the corresponding primary particles introduced at the top of the atmosphere. These matrices are parameterized by the zenith angle, defined as the angle between the trajectory of the incoming primary particle and the local vertical at the surface—that is, the angle at which particles are directed toward the surface. This approach allows us to assess how the Martian atmosphere modifies radiation transport as a function of particle injection angle. Once established, the matrices can be applied to any incident radiation spectrum—such as those from GCRs, SEPs, or other sources—by convolving them with the modeled response. We then present our simulation results and explain how we convolve the Geant4 output functions with both SEP and GCR spectra. This method enables accurate estimation of secondary particle fluxes generated in the atmosphere by primary protons in different zenith angles and arriving at the surface, provided the particle trajectories intersect the ground (i.e., for elevation angles greater than 0°). We also compare our results with other established models. The final chapter summarizes our findings and discusses their significance. In follow-up work, we will apply these results to develop a topographic radiation map of Mars, offering a detailed

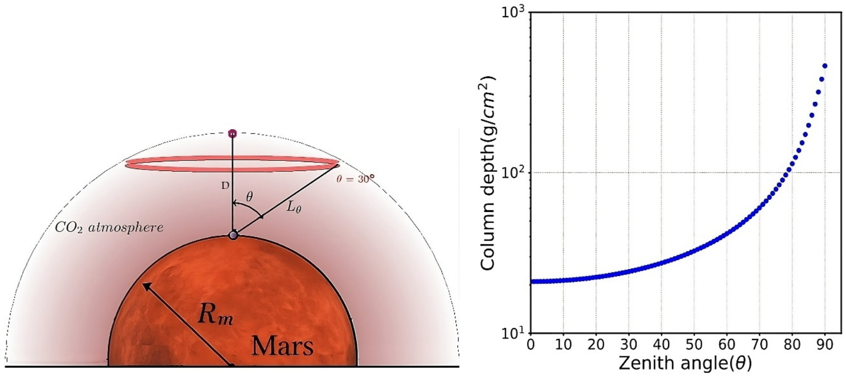

Figure 1. Left: Schematic view of a full-size spherical Mars as a substrate; and is a representation of the real-world system. The hemisphere of Mars is depicted in red. The position of Radiation Assessment Detector is indicated by a circle on top of surface. The red ring is an example of ring sources and the magenta point represents the source with θ equal to 0°. More information can be found in the text. Right: CO_2 column depth for different zenith angles on the surface of Mars (Adopted from (Khaksarighiri et al., 2023)).

view of surface-level radiation across varying terrains. This will help mission planners identify safer landing zones and improve shielding strategies for long-duration human presence on the planet.

2. Materials and Methods

2.1. Mars Atmospheric Model: Atmospheric Column Mass as a Function of Zenith Angle

We have employed a mathematical model to calculate the atmospheric column depth as a function of the zenith angle on the Martian surface. As a first step, we derived the column depth for varying zenith angles using a set of equations, with the left panel of Figure 1 serving as a reference. The left panel provides a full-scale, conceptual representation of Mars, accurately reflecting the physical properties of the Martian surface. The hemisphere of Mars is depicted in red, while the position of the RAD instrument on the surface is indicated by a circle. A red ring illustrates an example of ring-shaped particle sources, and the magenta point represents a directional source with a zenith angle θ equal to 0°. These sources simulate the incoming radiation flux at different orientations relative to the detector. The right panel shows the CO_2 column depth as a function of zenith angle on the Martian surface, illustrating how atmospheric shielding varies with the trajectory of incoming particles. This schematic highlights the combined effects of Martian surface geometry and atmospheric depth on particle interactions measured by RAD.

A key parameter influencing Martian atmospheric behavior is the atmospheric column depth, σ, which represents the integrated mass of the atmosphere along a given path. As illustrated in Figure 1, this depth increases with the zenith angle θ, as the path through the atmosphere becomes longer when moving from vertical to horizontal directions.

As illustrated in Figure 1, to geometrically estimate the path length through the Martian atmosphere, we model the line-of-sight from the surface to a given point in the atmosphere and apply the law of cosines:

$$(R_m + D)^2 = R_m^2 + L(\theta)^2 + 2R_m L(\theta)\cos(\theta). \tag{1}$$

Here, R_m is the radius of Mars, D is the vertical distance between the RAD instrument and the top of the atmosphere, and $L(\theta)$ is the effective atmospheric path length for a given zenith angle θ. Equation 1 is rearranged to solve for $L(\theta)$, yielding:

$$L(\theta) = -R_m \cos(\theta) + \sqrt{R_m^2 \cos^2(\theta) + D^2 + 2R_m D}. \tag{2}$$

This expression defines the effective slant path through the Martian atmosphere as a function of the zenith angle θ.

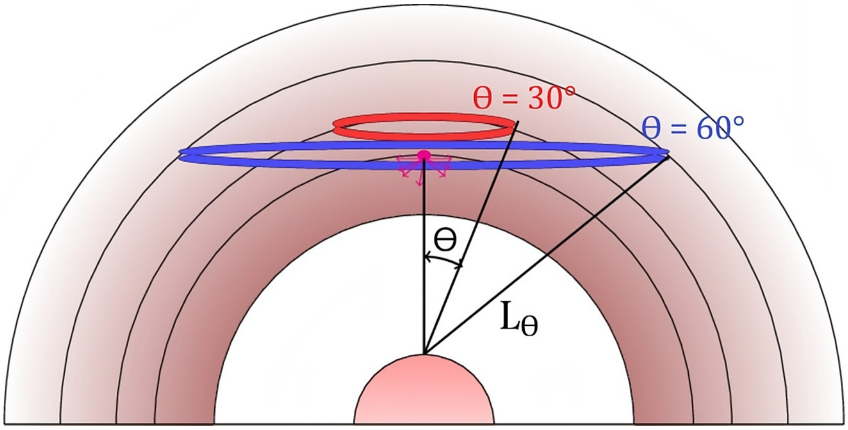

Figure 2. Schematic view of the zenith-angle (θ) dependence of the Mars atmospheric simulation setup (Adopted from (Khaksarighiri et al., 2023)). The red and blue rings are example ring sources with θ being 30° and 60°, respectively, and the magenta point represents the source with θ equal to 0°. More information can be found in the text.

To relate this path length to the atmospheric column depth, we adopt the barometric approximation for atmospheric density:

$$\sigma = \int_0^D \rho_0 e^{-h/H}\,\mathrm{d}h, \tag{3}$$

where ρ_0 is the atmospheric density at the surface, H is the atmospheric scale height, and h is the vertical height above the surface. Equation 3 defines the vertical column depth for $\theta = 0°$.

To extend this to oblique angles, we assume that the density remains roughly constant along a given path segment $L(\theta)$. Under this approximation, the atmospheric column depth can be estimated as:

$$\sigma(\theta) \approx \rho_0 \times L(\theta), \tag{4}$$

where $\sigma(\theta)$ is the slant column depth corresponding to zenith angle θ, and $L(\theta)$ is the effective path length computed from Equation 2.

As already mentioned, Figure 1 serves as a reference for the derivation of Equation 4 by illustrating the geometrical and physical relationships that connect the zenith angle θ, the effective atmospheric path length $L(\theta)$, and the column depth $\sigma(\theta)$. Figure 1 (right panel) displays the resulting $\sigma(\theta)$ values derived from this model. These values are then used to parameterize the atmospheric geometry in our simulation framework, as shown in Figure 2, where each hemisphere corresponds to a specific zenith angle and its associated column depth.

Figure 2 represent a schematic view of the zenith-angle (θ) dependence of the Mars atmospheric simulation setup used in our simulations. The Martian atmosphere in this figure is modeled as pure CO_2, reflecting the fact that carbon dioxide constitutes approximately 95% of its composition. The vertical column depth ($\theta = 0°$) of the atmosphere is approximately 21 g/cm^2, corresponding to an average surface pressure of about 800 Pa, as measured by REMS at Gale crater (REMS, Gómez-Elvira et al., 2012, Rover Environmental Monitoring Station). The column depth increases with an increasing θ angle toward the horizon, as demonstrated in the right panel of Figure 1. The angular distribution of radiation on the Martian surface is affected by interactions in the atmosphere, since particles approaching from near the horizon pass through much more material than those coming vertically. As a result, the interaction of SEPs and GCRs with the atmosphere leads to a change in the isotropic nature of the radiation field, which results in a higher directional flux of primary particles from the zenith than from the horizon.

Our model is set up to quantify the above effect and to determine the flux of secondary particles on the Martian surface from different zenith angles. To optimize our simulations, we adopted a compressed representation of the atmosphere. Instead of illuminating the entire top of the Martian atmosphere and tracking particles along extensive trajectories (most of which would not reach the detector) we initiated the atmospheric representation just 23 cm above the detector to accurately model the portion of the Martian atmosphere that directly interacts with incoming radiation at the measurement site. Additional CO_2 layers with increasing density were added to account for larger zenith angles, effectively simulating the longer atmospheric path lengths encountered by particles arriving from off-vertical directions. By extending the total column height to 162 cm, corresponding to a cumulative mass depth of 400 g/cm^2, the model captures the integrated shielding effect of the Martian atmosphere rather than just its geometric height. This approach ensures that both the vertical and angular dependence of the atmospheric column are realistically represented, providing an approximation of particle interactions and energy deposition in the vicinity of the detector while remaining computationally efficient. In this way, the model allows for the study of how incident particles at different angles experience distinct energy loss and secondary particle production as they propagate through the Martian atmosphere.

The detector is modeled as a hemisphere with a radius of 5 cm placed on the surface of Mars. To validate this setup, we performed simulations for two scenarios, in which particles originate at different distances above the detector: 25 cm, corresponding to the position of the first CO_2 layer, and 100 cm. In both cases, the particles are emitted at the same zenith angle. These simulations are intended to verify that the number of particles reaching the detector is consistent when considering particles that have already exited the CO_2 layers and no longer undergo interactions, ensuring that the detector effectively records the relevant flux. After normalizing the data to the primary source flux, we observed a negligible difference of less than 4% between these two simulations, confirming the validity of our approach. σ calculated in Equation 4 represents the column depth of the atmosphere, which increases with the zenith angle from vertical to horizontal directions, as shown in Figure 1. The gray scale in Figure 2 represents the Mars atmosphere which is set to be 100% CO_2 in this model. The red and blue rings are example sources with θ being 30° and 60° placed in various layers with corresponding column depth of atmosphere, respectively. The magenta point represents the source with θ equal to 0° corresponding to 21 g/cm^2 of CO_2, placed on top of the first layer of CO_2 with 30 cm of radius. The detector itself has been placed in a high vacuum hemisphere, which means all the primary and secondary particles will follow their direction, after passing through the CO_2 layers. In this model, the zenith angle does not directly reflect the actual zenith angle of particles at the Martian surface. The assumption is that the zenith angle of a particle reaching the surface is the same as that of the primary particle at the top of the atmosphere. In other words, particles from different angular rings are assumed not to mix or cross into one another during their passage through the atmosphere.

Due to the interaction of particles with the atmosphere at the uppermost layer of Mars' atmosphere, they deviate from the black line labeled L_θ in Figure 2. These particles can undergo ionization process, leading to energy loss, and, if they possess sufficient energy, they may generate secondary particles or even initiate a cascade of secondary particle production. Our methodology involved placing primary particle sources along distinct spherical segments, each characterized by a constant zenith angle. These segments are visually depicted as the red and blue rings at $30^\circ \pm 1^\circ$ and $60^\circ \pm 1^\circ$ in Figure 2, respectively.

Particle emissions were initiated from the inner surface of each ring, following an inward cosine-directional distribution with a spectral power-law index of -1. This configuration yields an isotropic and homogeneous particle field within the sphere, as illustrated by the red arrows for the magenta source primary protons were assigned a range of modeled energy spanning from 1 MeV to 100 GeV and distributed across 50 logarithmically spaced bins. This approach facilitates subsequent re-binning and enables the convolution of our modeling results with various GCR and SEP spectra, as detailed in Section 3.1. For each zenith angle, a total of 5×10^7 particles were simulated, corresponding to 10^6 particles per energy bin. However, for the 90° zenith angle, we performed simulations with 1.5×10^6 particles to ensure more robust statistical results, as most particles are stopped by the CO_2 column depth before reaching the detector.

2.2. Geant4 Toolkit

Geant4 (version 10.7.4), a robust three-dimensional Monte Carlo particle transport toolkit, was employed in this study. The simulations were performed using the `QGSP_BERT_HP` physics list, which provides detailed modeling of electromagnetic and hadronic interactions, including high-precision neutron transport. This physics list uses the standard electromagnetic physics (`G4EmStandardPhysics`), providing accurate treatment of electromagnetic interactions such as ionization, bremsstrahlung, Compton scattering, and pair production.

Geant4 (Agostinelli et al., 2003) provides a comprehensive set of tools for simulating the passage of particles through matter. It includes a geometry description package that allows users to define the physical and material properties of the target, as well as the placement and orientation of detectors. The QGSP BERT physics list encompasses the quark-gluon string model for high-energy particles (with energies equal to or greater than 20 GeV) and the Bertini cascade model tailored for middle and low-energy ranges. Within this framework, excited nuclei generated by high-energy interactions are directed to the percompound model, which is used to describe the de-excitation process. The high precision (HP) component refers specifically to the HP Neutron Package in Geant4, which is designed to handle low-energy neutron interactions (typically below 20 MeV) with high accuracy. In modeling the Martian radiation environment, it has been found that different physics lists can affect the generation of secondary particles, especially those produced via spallation processes (Guo, Banjac, et al., 2019). However, the surface absorbed dose agrees within ∼5% for different physics lists (Matthiä et al., 2016).

3. Simulation Results and Comparison With Previous Studies

3.1. Procedure of the Model Application

As previously mentioned, in our simulations, we consider only protons as the primary source above the Martian surface, emitting particles isotropically from different rings at varying zenith angles and recording all secondary particles that reach the surface. We then construct a lookup table representing the ratio of secondaries to primary particles upon reaching the surface, which can be used to convolute with SEP or GCR proton spectra in deep space and on the surface of Mars.

Figure 3 visually summarizes the process of incorporating SEP fluence to calculate the flux of secondary particles generated on the surface of Mars using Geant4 simulation results. The figure also presents the outcomes for proton flux on the Martian surface at various zenith angles, serving as an illustrative example.

Figure 3a shows the simulation results from Geant4 for the fluence ratio of secondary protons produced at the Martian surface relative to the input primary proton fluence used in the simulation. This ratio is presented as a function of secondary particle energy E', for several zenith angles θ, and is integrated over all primary energy bins. These ratios effectively represent a transfer function $F_m(E', E, \theta)/f(E)$, indicating how efficiently incident protons of varying energies contribute to secondary production at different angles.

Figure 3b shows the GCRs in various solar modulations as well as the reconstructed SEP event of 15 February 2022, analyzed by (Zhang et al., 2024) at the vicinity of Mars. This wide spread SEP event was observed at multiple locations in the inner heliosphere, including Earth, Mars, STEREO-A, Parker Solar Probe, and Solar Orbiter. This event was associated with a fast coronal mass ejection exceeding 2,300 km/s at 25 solar radii (Khoo et al., 2024). Although not directly aimed at Mars, its flank was likely magnetically connected to the planet, as indicated by the increased proton flux observed by surface and orbital detectors (Zhang et al., 2024). Given its broad observational coverage and significant impact, we use this event to convolve with our functions and analyze SEP effects on the Martian surface.

To compute the resulting surface flux from a specific SEP event, we multiply this transfer function with the input SEP proton spectrum $F(E)$, shown in Figure 3b. This operation integrates over the primary energy E, yielding the expected secondary flux $\dot{F}(E', \theta)$ at the Martian surface. The resulting spectra for different θ values are shown in Figure 3c. This methodology can be extended to calculate surface fluxes for various secondary particle species and incident angles.

Mathematically, this procedure is summarized in Equation 5:

$$\dot{F}(E', \theta) = \int \left[\frac{F_m(E', E, \theta)}{f(E)} \right] \cdot F(E)\, dE, \tag{5}$$

where:

- $F_m(E', E, \theta)$ is the fluence of secondary particles of species m (e.g., protons) with energy E', produced by primaries with energy E and incident angle θ, as obtained from Geant4 simulations, in units of particles per cm^2 MeV;

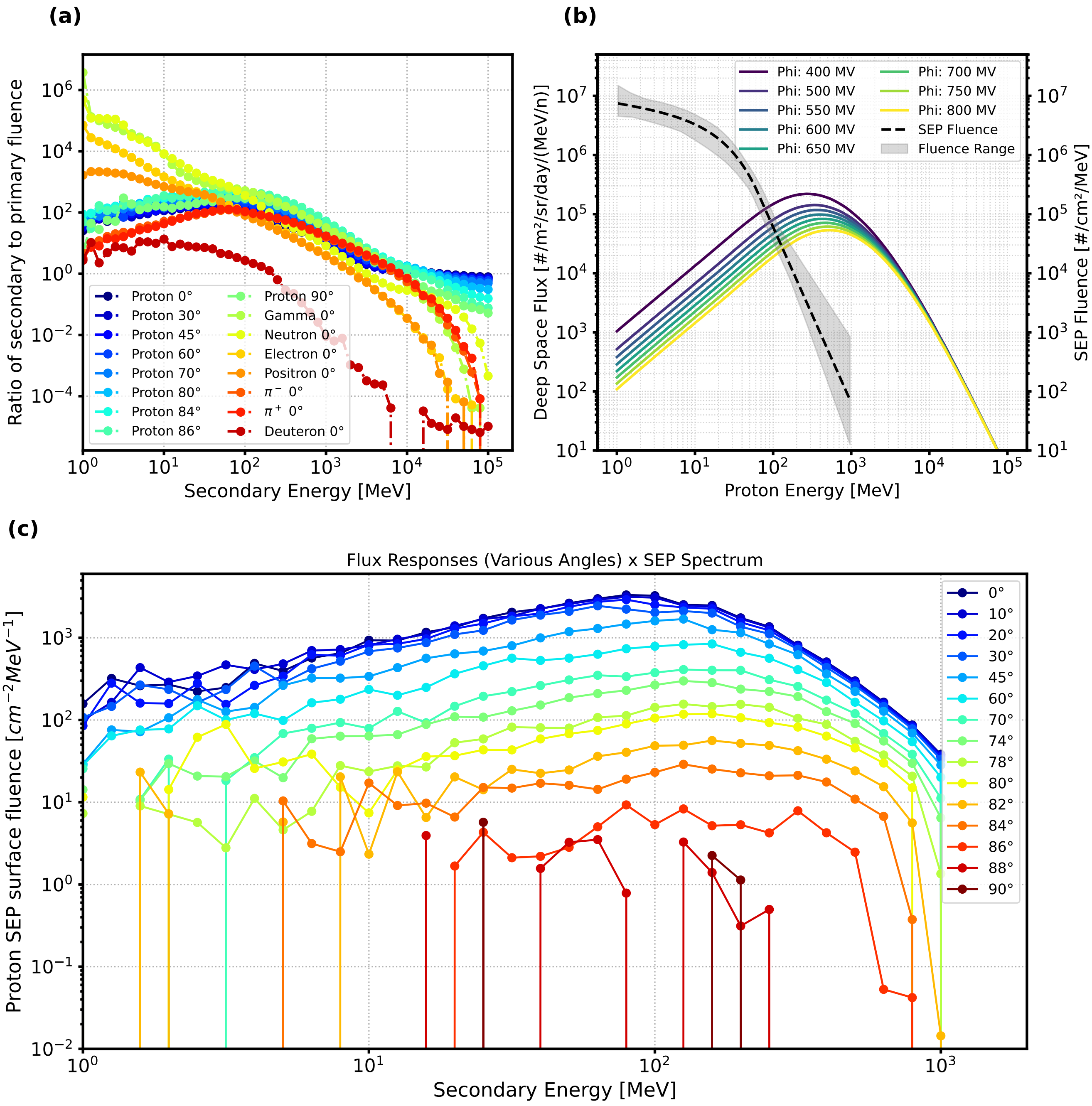

Figure 3. Convolution of the pre-calculated flux ratio functions with input Solar Energetic Particle (SEP) spectra to calculate the Martian surface flux of various species. Panel (a) presents the ratio of secondary particles produced in the simulations to the incident primary proton fluence for the 0° zenith-angle configuration. This ratio is calculated in discrete energy bins and is displayed here after integration over all primary energies. (b) Represents the Galactic Cosmic Rays in different solar modulations and reconstructed SEP event of 15 February 2022, The maximum and minimum values of the SEP spectra, represented by the shaded area, reflect the full range of 10,000 Band function fits that account for uncertainties the reconstructed spectra (Zhang et al., 2024). Finally, panel (c) illustrates the results of convolving the flux-response functions with the SEP spectrum from panel (b) in each corresponding energy bin and subsequently integrated over all primary energy bins. More details can be found in Section (3.1).

- $f(E)$ is the normalized input primary fluence spectrum used in the simulation in unit of particles per cm^2 MeV;
- $F(E)$ is the SEP event oR GCR spectrum, in units of particles per cm^2 MeV;
- $\dot{F}(E',\theta)$ is the resulting surface flux of secondaries at energy E' and angle θ, in units of particles per cm^2 MeV.

This equation represents a convolution over the primary energy *E*, in which the incident SEP and GCR spectra is transformed into the resulting secondary particle spectrum at the Martian surface, using a response function obtained from the Geant4 simulations.

Figure 3c presents the variation in proton fluence on the Martian surface as a function of secondary energy for different zenith angles, ranging from vertical (0°) to horizontal (90°) particle incidence. As already mentioned the data were obtained by convolving pre-computed response functions with the reconstructed SEP spectrum from the solar event on 15 February 2022. The results show that as the zenith angle increases, the overall proton fluence decreases, especially at lower and higher energies. This is primarily due to the longer atmospheric path length particles must traverse at oblique angles, leading to greater attenuation and reduced surface penetration. The peak fluence appears near 100 MeV for more vertical angles and gradually diminishes with increasing angle. Sharp drops or gaps in fluence at larger angles are also evident, which may reflect geometric constraints or atmospheric shielding effects. This analysis underscores the significance of zenith angle in shaping the radiation environment on Mars and highlights the need to consider angular dependence when modeling surface radiation exposure during solar particle events. Subsequently, utilizing this data, we create lookup tables that depict the varied flux of secondary particles. Employing these matrices alongside the incident spectrum enables the calculation of secondary particle flux from all zenith angles on the Martian surface.

In the following sections, we compare our results with previous studies that have estimated the surface flux of secondary particles on Mars (Guo, Banjac, et al., 2019; Matthiä & Berger, 2017; Charpentier et al., 2024). To facilitate this comparison for the SEP and GCR spectra, we calculate the total downward flux in our study by integrating the flux of secondary particles reaching the Martian surface from different zenith angles. To compute the integral of the flux over the full 360° azimuth and 0°–90° zenith angle range (i.e., downward-directed particles on the Martian surface), we sum the contributions from each differential solid angle, weighted by the corresponding flux values. This calculation is performed for zenith angles between 0° and 90°, after which the result is multiplied by 2π to account for the half-sphere of the azimuthal distribution.

3.2. SEP-Induced Secondary Particle Fluence on the Martian Surface

In this part, the interaction of primary solar energetic protons with the Martian atmosphere was modeled to assess the resulting secondary particle fluence on the surface of Mars. The simulations considered various Martian atmospheric shielding in different zenith angles and involved a convolution of the resulting surface response functions with a representative SEP proton event spectrum. To implement this methodology, our model confines the primary particles to distinct rings, as detailed in Section 2.1, at various zenith angles. These angles correspond to different column depths of the Martian atmosphere's surface, enabling the calculation of secondary particle fluxes resulting from particle interactions with the atmosphere and their subsequent arrival at the Martian surface from different zenith angles. The resulting differential fluences for various secondary particle species such as gamma rays, electrons, neutrons, and protons are presented as a function of secondary energy, with corresponding uncertainty bands.

Figure 4 shows the modeled fluxes of various particle species—gamma rays, electrons, neutrons, and protons—reaching the Martian surface, along with comparisons to the Atmospheric RAdiation Model for Ionizing Spectra on the Martian Surface (ARAMIS) model and RAD measurements for protons. The results from our model were obtained by convolving the simulated particle transport data for each species with the observed SEP spectrum from the 15 February 2022 event, yielding integrated fluxes. This convolution approach enables an effective translation of the incident SEP spectral characteristics into surface-level response functions representative of the Martian radiation environment.

The shaded regions in different panels of Figure 4, represent the full range of possible SEP spectra derived from 10,000 realizations of the Band function, each incorporating variations in the model parameters. These realizations are used to capture the uncertainties inherent in the spectral fits of the primary proton spectrum at Mars, and the resulting envelope—bounded by the maximum and minimum values across all simulations—effectively illustrates the spectrum's statistical spread. This approach provides a robust quantification of the uncertainties associated with the SEP spectral shape and intensity, ensuring that both the central trend and the variability of the input spectrum are adequately represented in the subsequent analysis (Zhang et al., 2024).

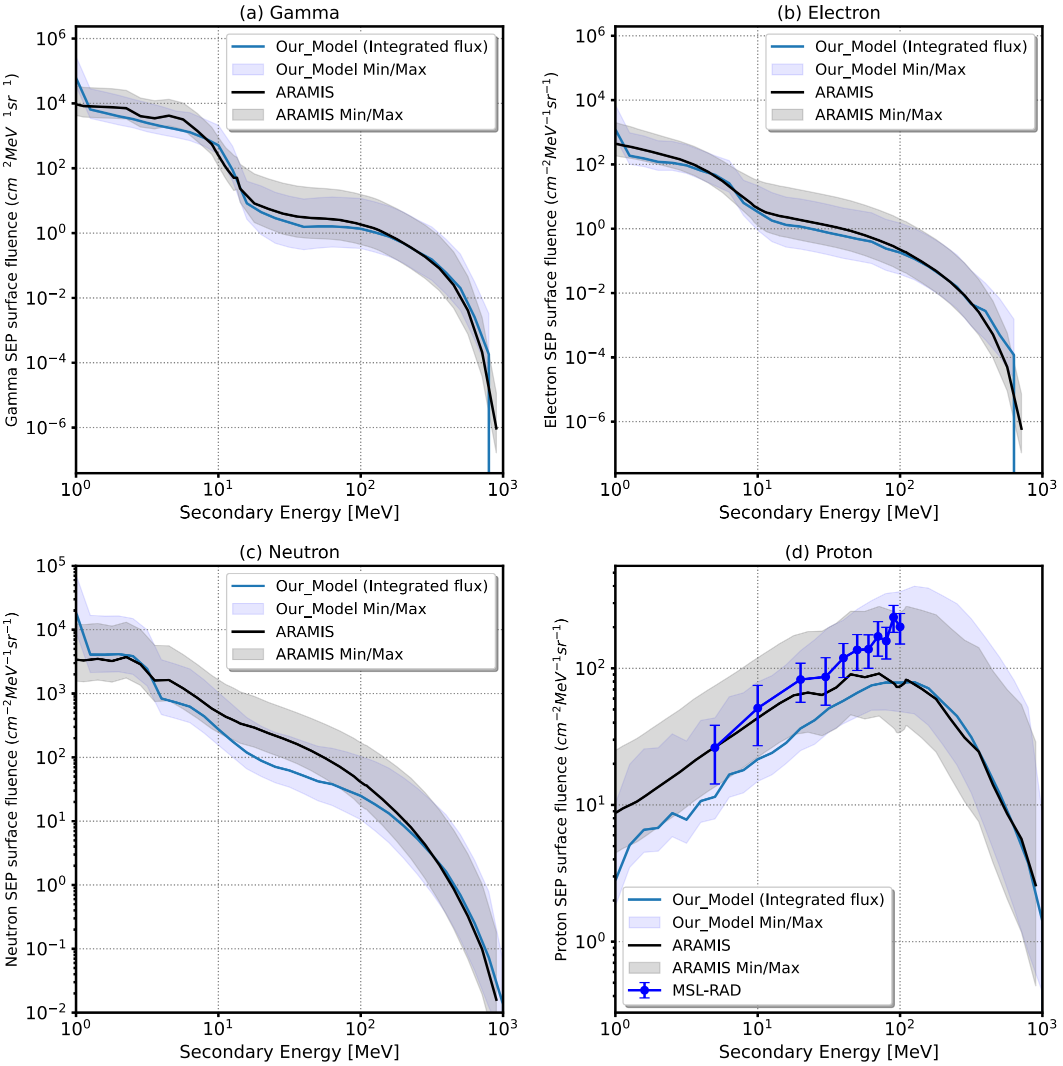

Figure 4. Integrated flux of secondary particles induced by the February 2022 Solar Energetic Particle (SEP) event on the Martian surface, as calculated using our model and Atmospheric RAdiation Model for Ionizing Spectra on the Martian Surface for different particle types: (a) Gamma, (b) Electron, (c) Neutron, and (d) Proton. The proton results are additionally compared with Radiation Assessment Detector measurements. The shaded regions in each panel represent the full range of possible SEP spectra obtained from 10,000 realizations of the Band function, each incorporating variations in the model parameters.

To further validate and compare our findings, we employed the same input SEP spectral distribution in the ARAMIS model—a well-established framework for simulating particle transport in planetary atmospheres (Charpentier et al., 2024)—to calculate the corresponding surface fluxes of the same particle species on Mars. ARAMIS is a computational framework designed to efficiently simulate radiation transport and particle interactions in the Martian atmosphere. ARAMIS employs a response-function methodology, allowing for rapid recalculations of surface fluxes for varying input spectra of GCRs and SPEs. This approach significantly enhances computational efficiency while maintaining accuracy. Built upon Monte Carlo simulations, ARAMIS has been validated against observational data from the RAD, as well as against previous radiation transport models. The model leverages GEANT4-based simulations with the FTFP_INCLXX_HP physics to reconstruct the particle flux at the Martian surface, employing a response-function technique that preserves the structural integrity of the results while offering flexibility in exposure scenario modeling (Charpentier et al., 2024).

By implementing this approach, we computed and compared the resulting spectra of different species for the SEP event on the Martian surface in Figure 4. Our findings agree well with the ARAMIS model in multiple species, as illustrated in Figure 4. This consistency reinforces the reliability of our model in accurately reproducing the behavior of energetic particles in the Martian environment. As shown in this figure, the ARAMIS model predicts higher fluxes for most particle species in the 10–100 MeV energy range, except for protons, which our model shows a higher surface flux over 50 MeV. The observed differences can likely be attributed to variations in the underlying physics models of GEANT4 and assumptions between the two simulation frameworks, particularly in terms of the atmospheric interaction modeling, and the angular dependence of particle transport. Additionally, our simulations account for angular effects by running at various zenith angles and integrating the resulting fluxes over the upper hemisphere, thereby capturing the influence of different atmospheric path lengths encountered by inclined particles. The ARAMIS results were also refined by simulating monoenergetic primary particles with energies from 70 MeV (below the cutoff) to 1 GeV in 10 MeV increments, followed by convolution with input spectra to obtain the realistic surface flux. The modeling results are also validated against RAD measurements, as shown in the proton panel. Here, we use the stopping proton fluxes observed by RAD for the same event. Determining the onset time of SEP impact on the stopping flux is limited by the narrow field of view of RAD's geometry factor. The measured fluxes are scaled by a factor of 2π divided by the Solid angle of the RAD view cone to estimate the flux over the full 2π steradians and enable direct comparison with the modeling results.

The results show characteristics of secondary particle production on the Martian surface in response to SEP events. Notably, the SEP-induced secondary fluence leads to significant surface fluxes of gamma rays, electrons, and neutrons at low energies. This is particularly notable given that the corresponding primary proton spectrum exhibits minimal intensity in the same low-energy range. SEP events can also produce elevated fluxes of low-energy secondary particles at the surface. This is primarily attributed to the ability of high-energy primary protons to penetrate the atmosphere and initiate nuclear interactions—particularly spallation reactions—which generate cascades of secondary particles. Consequently, even when the low-energy component of the primary spectrum is negligible or absent at the Martian surface due to the atmospheric column depth and the atmospheric cutoff energy for primary protons on Mars being approximately 160 MeV/nuc as reported by (Guo, Wimmer-Schweingruber, et al., 2019), protons with energies below this threshold are largely stopped by the atmosphere at Gale Crater, which has an average depth of about 21 g/cm^2 of CO_2. Nonetheless, the secondary particle spectrum can still exhibit significant enhancements at low energies resulting from atmospheric cascade processes initiated by higher-energy primary protons. This behavior underscores the complex interplay between the energy distribution of primary SEPs and the resulting secondary radiation environment on the Martian surface. It highlights the need to account not only for the direct transport of primary particles but also for the indirect generation of secondary radiation when evaluating surface radiation exposure risks.

Furthermore, to assess the influence of primary particle directionality on secondary particle production, we employed the ARAMIS model to simulate proton propagation with an incident zenith angle of 0°. By considering a flux of protons coming vertically at the Martian surface, we calculated the resulting spectra of various secondary particles generated through interactions with the atmosphere in Figure 5. Panel (a) presents the gamma fluence, representing the surface gamma flux produced by secondary atmospheric interactions, where both models exhibit good overall agreement, with only minor deviations at intermediate energies. Panel (b) shows the electron fluence, corresponding to the energy spectrum of secondary electrons, with similar spectral shapes and magnitudes in both models, reflecting a consistent treatment of electromagnetic cascades. Panel (c) illustrates the neutron fluence arising from nuclear interactions, demonstrating strong agreement at higher energies, with minor discrepancies at lower energies. Finally, panel (d) displays the proton fluence, characterizing the surface flux of secondary protons. Despite methodological differences, such as the use of different physics lists and modeling approaches, the results from the vertical incidence case in Figure 5 show overall agreement with our model's predictions, highlighting the robustness of our approach in reproducing the key features of secondary particle production on the Martian surface. To reduce uncertainties in the low-energy range of the surface proton flux, the ARAMIS input spectrum was refined with an energy resolution of 10 MeV between 70 MeV (below the atmospheric cutoff) and 1 GeV.

This analysis highlights the consistency of our simulation framework in capturing the spectral characteristics of secondary radiation under different primary particle incidence conditions.

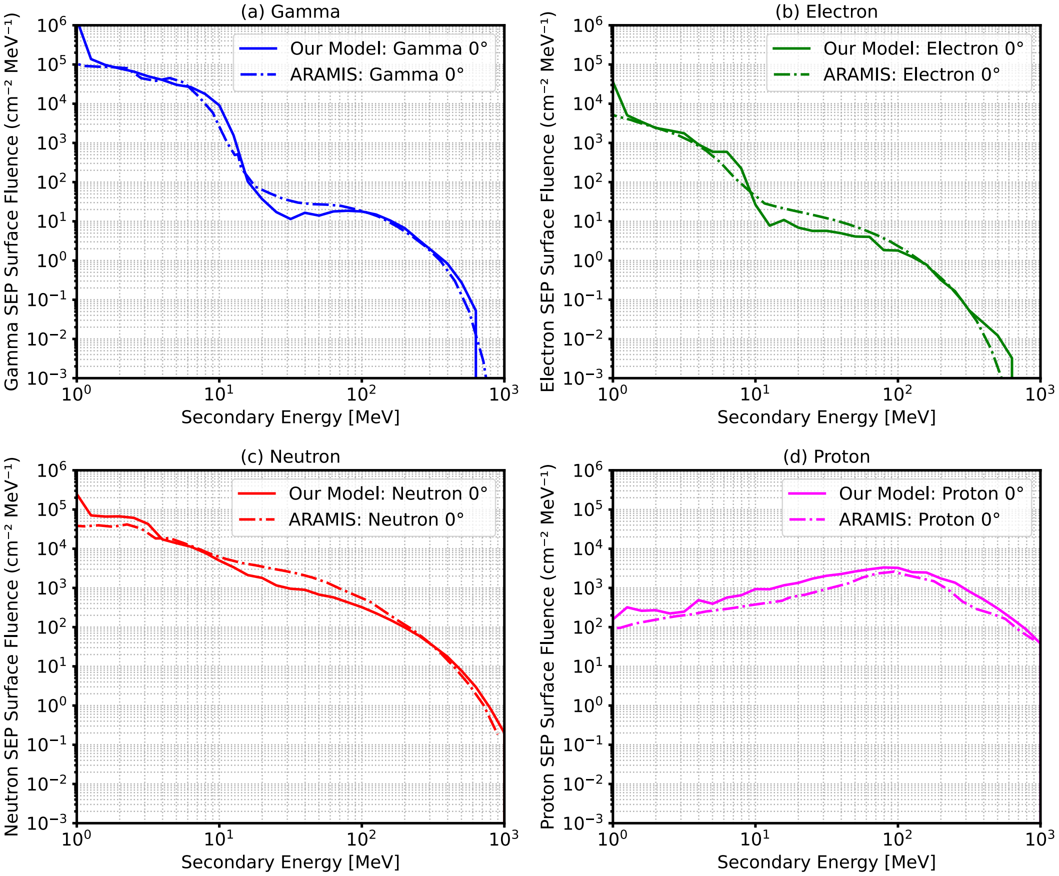

Figure 5. Fluxes of secondary particles induced by the February 2022 solar Solar Energetic Particle event on the Martian surface, evaluated using both our model and the Atmospheric RAdiation Model for Ionizing Spectra on the Martian Surface framework for primary particles entering vertically (0° incident angle) at the top of the atmosphere. Panels show the resulting surface fluxes for (a) gamma, (b) electron, (c) neutron, and (d) proton species.

3.3. Spectra of Different Particle Species From GCRs at Various Zenith Angles on the Surface of Mars

Here, we apply the same procedure for GCRs on the Martian surface as described in Section 3.2 for SEPs. The resulting particle fluxes on the Martian surface are presented in Figures 6 and 7.

Figure 6 shows the flux of protons reaching the surface of Mars for different zenith angles, folded with GCR spectra with a solar modulation of 400 MV. Since the primary source consists of protons, this figure specifically illustrates the proton flux, including contributions from both primary cosmic rays and secondary particles produced in the Martian atmosphere. The variation with zenith angle highlights the angular dependence of the surface proton environment, which is shaped by atmospheric shielding and particle cascades.

The plot in Figure 6 reveals an angular dependence of the surface proton flux under GCR conditions. For vertically incident protons (0°), the surface flux is highest across nearly the entire energy range, particularly between 100 MeV and several GeV. This outcome is expected, as particles arriving at normal incidence encounter the shortest atmospheric path length and are thus least attenuated. As the zenith angle increases, the path through the Martian atmosphere lengthens, effectively increasing the atmospheric column depth and enhancing both energy loss and absorption, resulting in a significant reduction in the surface proton flux—especially at low energies. For extreme angles near the horizon (88°–90°), this attenuation is most pronounced, with fluxes dropping by several orders of magnitude below 100 MeV.

Interestingly, the spectra for intermediate zenith angles (particularly below 74°) suggest that an increase in column depth may initially enhance secondary particle production due to a higher probability of nuclear interactions along the extended path. These secondaries, particularly low-energy protons produced via spallation

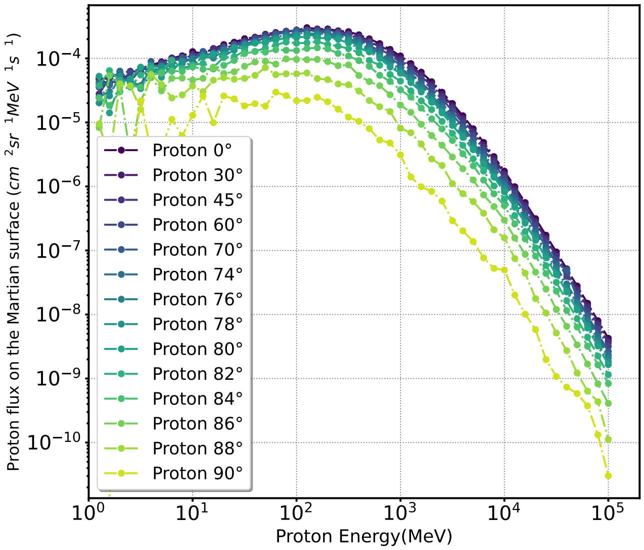

Figure 6. Primary and secondary proton spectra generated only by primary protons reaching the Martian surface at various zenith angles modeled in this study.

and inelastic collisions, can contribute to an elevated surface flux in the mid-energy range (100 MeV to a few hundred MeV). This effect gradually diminishes at larger zenith angles, where the increasing atmospheric shielding outweighs the additional secondary production, leading to an overall suppressed flux at the surface.

The other species shown in the panels of Figure 7 represent secondary particles generated exclusively by the interaction of primary protons—assumed as the only incident GCR species in our simulations—with the Martian atmosphere. These particles include gamma rays, electrons, neutrons, positrons, positive pions (π+), and deuterons. The surface fluxes are shown as a function of energy for a wide range of incident zenith angles, from vertical (0°) to near-horizontal (90°).

The effect of zenith angle on the surface flux of these secondary particles is markedly less pronounced than for protons (as shown earlier in Figure 6). This is expected, as most of these secondaries are produced in situ at various depths in the atmosphere rather than being primary particles incident from space. Consequently, their flux at the surface depends more on the integrated particle production and transport through the atmosphere than on the initial direction of the primary protons.

For gamma rays, electrons, and neutrons, the fluxes show relatively modest angular variation across the entire energy spectrum. These species are pre-

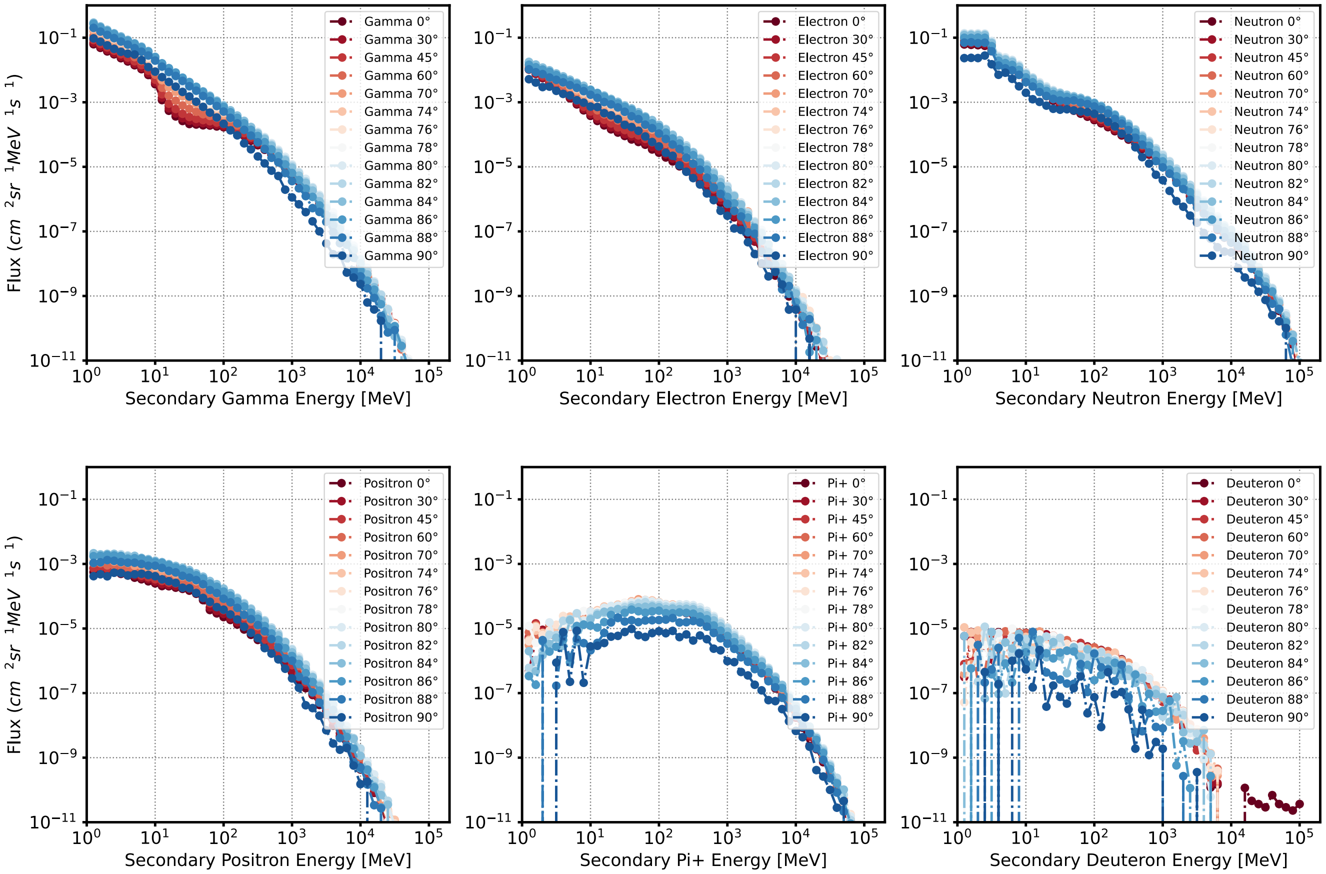

Figure 7. Secondary particle spectra reaching the Martian surface at various zenith angles, derived from primary protons and folded with Galactic Cosmic Rays at 400 MV solar modulation. The spectra include secondary gamma rays, electrons, neutrons, positrons, deuterons, and tritons.

dominantly produced through electromagnetic and hadronic cascades and have relatively long interaction lengths or large angular spreads due to scattering processes. Therefore, their generation is more distributed across the atmospheric column, and their flux at the surface remains relatively isotropic, especially at lower and intermediate energies. The observed attenuation at the highest zenith angles (88°–90°) is present but not as significant as for protons.

The dip observed in the gamma-ray spectrum between 10 and 100 MeV, as illustrated in Figure 4 of Fujiwara et al. (2025), arises from the transition between distinct dominant gamma-ray production mechanisms. At photon energies $E_\gamma \lesssim 10$ MeV, gamma-rays are mainly produced by nuclear de-excitation and radioactive decay, which give rise to distinct line features. In contrast, at $E_\gamma \gtrsim 100$ MeV, the spectrum is dominated by hadronic decays, primarily $\pi^0 \rightarrow \gamma\gamma$, which create a smooth high-energy continuum. In the intermediate range, bremsstrahlung from secondary electrons contributes a broad, but relatively weak, flux that does not connect the low- and high-energy components. Consequently, the combined spectrum exhibits a relative minimum, or "dip," in the 10–100 MeV range, where neither nuclear de-excitation nor hadronic decay is the primary emission process.

In contrast, positrons exhibit a slightly stronger dependence on the zenith angle, particularly at higher energies, though still less pronounced than for protons. This may be attributed to the fact that positron production is closely tied to electromagnetic cascades initiated by secondary gamma rays, which themselves originate from hadronic and nuclear interactions. The overall flux remains more uniform than that of primary-origin particles due to the broader angular distribution and multiplicity of production channels.

The behavior of positive pions and deuterons is notably different. Both species show distinct spectral shapes and more pronounced angular trends. For $\pi+$, the surface flux is generally low and shows a peak in the few hundred MeV range. The flux decreases with increasing zenith angle, indicating that their production is more forward-peaked and less efficient at larger angles due to increased atmospheric path lengths and energy losses. Similarly, deuterons, which are rare fragments produced through nuclear spallation, exhibit sharp drops at high zenith angles, with a highly structured and low-statistics spectrum. Their flux is significantly suppressed beyond 1 GeV for oblique angles, reflecting both their low production probability and high attenuation in the extended atmospheric path.

As mentioned above, to compare our results with RAD measurements and previous studies that have estimated the surface flux of secondary particles on Mars such as the Atmospheric Radiation Interaction Simulator (AtRIS), The PLANETOCOSMICS toolkit and ARAMIS (Guo, Banjac, et al., 2019; Matthiä & Berger, 2017; Charpentier et al., 2024), we computed the total downward flux by integrating the flux of secondary particles reaching the Martian surface across different zenith angles.

AtRIS (Banjac et al., 2019; Guo, Banjac, et al., 2019) is a specialized GEANT4 model designed to simulate the interaction of radiation with planetary bodies. This particle transport code has been meticulously developed to offer unparalleled flexibility in specifying planetary details, including atmosphere and soil geometry, composition, and more. Its adaptability makes it particularly suitable for modeling the radiation environment of exoplanets. AtRIS has been employed with a tailored implementation of the Martian atmospheric and regolith structure to accurately model the radiation environment on Mars. The results obtained from AtRIS are benchmarked against the energetic particle spectra measured by RAD on the Martian surface, affirming its reliability and precision in capturing real-world data (Guo, Banjac, et al., 2019).

The PLANETOCOSMICS toolkit (Desorgher et al., 2006) is an adapted version of GEANT4. In PLANETOCOSMICS, particle transport through the simulated Martian environment is performed with GEANT4.10.01.p03. For inelastic hadronic interactions, the toolkit employs the Liege Intra Nuclear Cascade Model for intermediate energies (<20 GeV for protons and neutrons, <12 GeV for alphas, <54 GeV for heavier nuclei) (Boudard et al., 2013). At higher energies, the Fritiof-Percompound (FTFP) model is used (Andersson et al., 1987). For neutrons below 20 MeV, the GEANT HP model applies an evaluated neutron data library (G4NDL) based on ENDF/B-VI data (Rose, 1991), and the ARAMIS model has already been explained in Section 3.2.

As discussed in Section 3.1, our function was convolved with GCRs using a solar modulation parameter of 400 MV. For comparison, we employed AtRIS data modeled under the same solar modulation condition. PLANETOCOSMICS/GEANT4 simulations used primary GCR nuclei with atomic numbers ranging from $Z = 1$ to 28, encompassing elements from hydrogen to nickel. The corresponding energy spectra were modeled

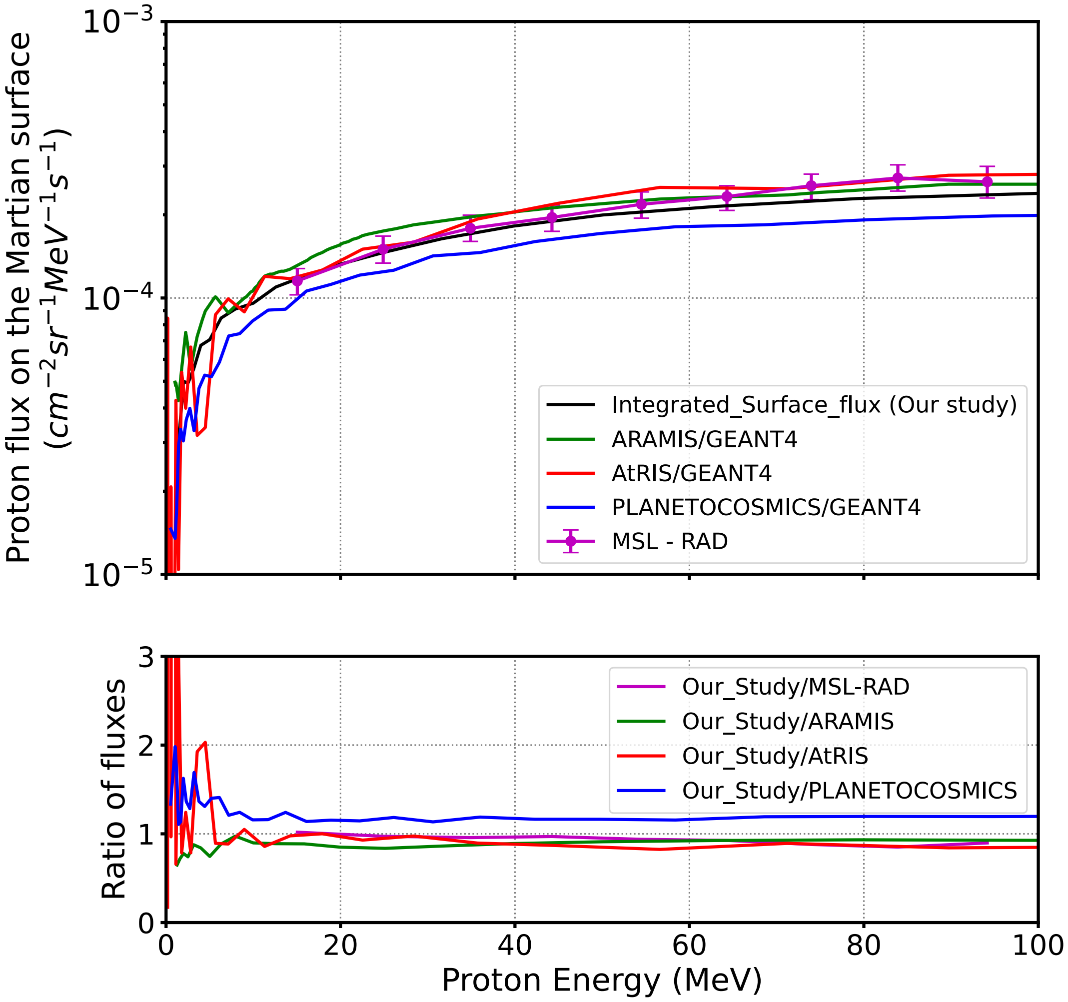

Figure 8. Comparison of our results with Radiation Assessment Detector measurements, as well as Atmospheric Radiation Interaction Simulator, PLANETOCOSMICS, and Atmospheric RAdiation Model for Ionizing Spectra on the Martian Surface. The plotted results are restricted to this energy range to enable a direct comparison and ensure an accurate ratio calculation.

following the approach of Matthiä et al. (2013) for the period from 15 November 2015, to 15 January 2016, during which the GCR intensity was at an intermediate level, following the minimum observed after the relatively weak solar maximum at the end of 2014 and the beginning of 2015. Given that solar modulation fluctuates between 300 and 1200 MV throughout the solar cycle, the modulation values applied by PLANETOCOSMICS/GEANT4 during this period align with those used in our study, thereby reinforcing the comparability of our results.

Figure 8 presents a comparison of our results, expressed as the integrated surface flux (Our study), with RAD measurements, as well as with the results reported by (Guo, Banjac, et al., 2019; Matthiä & Berger, 2017; Charpentier et al., 2024). The downward fluxes were calculated using AtRIS, PLANETOCOSMICS, and ARAMIS, respectively, as previously discussed for protons. The lower panels illustrate the ratio of our results to those from each of these studies, demonstrating a consistent level of agreement. Since RAD measurements are limited to energies below 100 MeV, we have restricted our plotted results to this energy range to enable a direct comparison and ensure an accurate ratio calculation. In the upper panel, our integrated surface flux (black line) is shown to align closely with the RAD data (purple points with error bars), particularly for proton energies above approximately 20 MeV. The fluxes computed using different transport codes show some variation at lower energies but converge within a factor of 2 across the energy spectrum considered. Notably, our simulation results fall well within the experimental uncertainty bounds provided by RAD, which reinforces the validity of the employed modeling framework. The lower panel provides a ratio-based comparison of our results to the other referenced

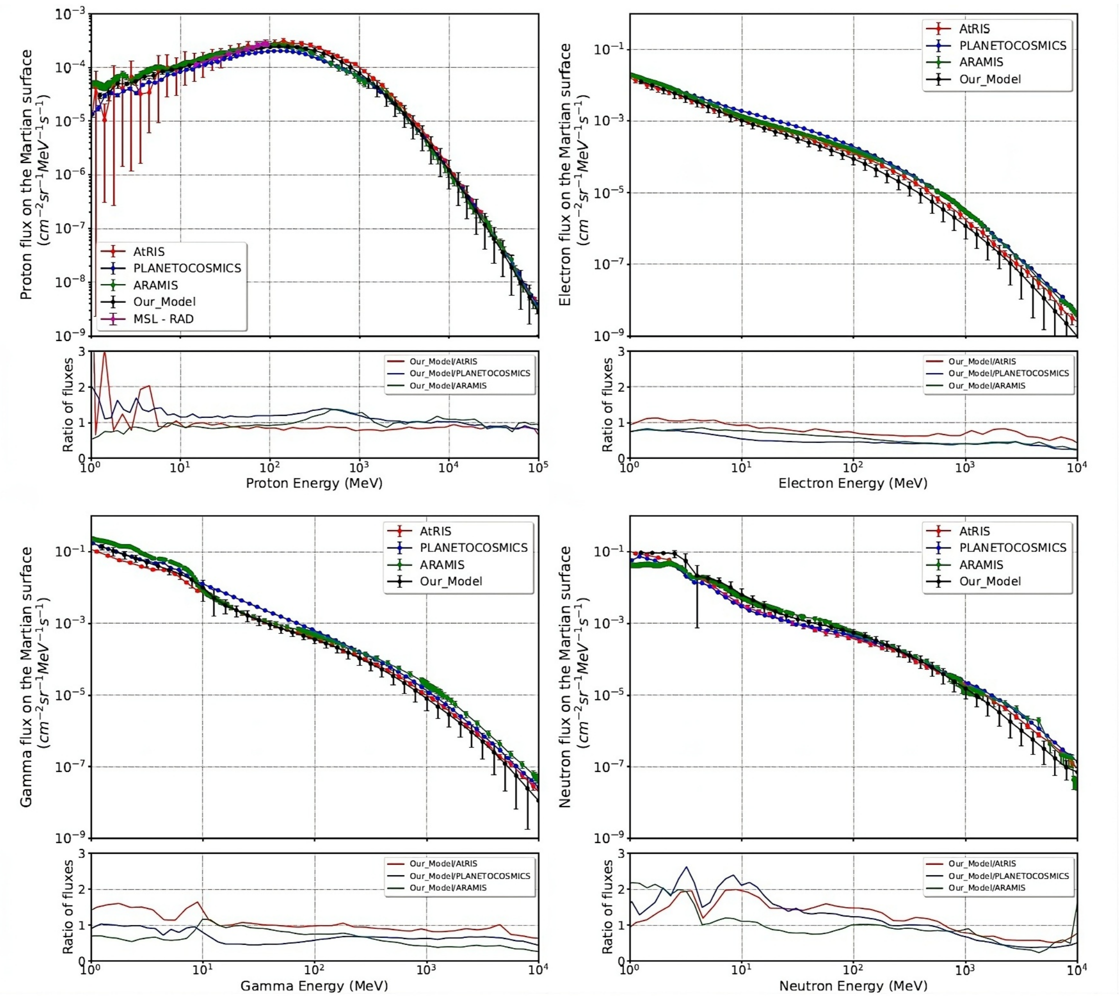

Figure 9. Comparison of our Galactic Cosmic Ray (GCR) flux integrated over the entire 2π with those reported in (Guo, Banjac, et al., 2019; Matthiä & Berger, 2017; Charpentier et al., 2024) for proton, electron, gamma, and neutron spectra reaching the Martian surface. The lower panel in each figure shows the ratio of the integrated GCR flux in our results for downward particles to those from other models.

models. The ratio remains close to unity over most of the energy spectrum, particularly in the 10–100 MeV range, further emphasizing the good agreement. Deviations below 10 MeV can be attributed to differences in physics used in the models, atmospheric modeling assumptions, or primary spectrum implementations in the respective models.

The upper panels of Figure 9 present a comprehensive comparison of secondary particle fluxes—protons, electrons, gamma rays, and neutrons—on the Martian surface, as calculated using our model, the AtRIS model, and the PLANETOCOSMICS model, along with ARAMIS. For protons, observational data from the MSL-RAD instrument are also included, enabling direct validation against in situ measurements. Across the entire energy range considered, a generally good agreement is observed among the models, with only minor deviations, particularly at low and high energy extremes. Notably, the proton fluxes predicted by our model align closely with those derived from MSL-RAD data. For electrons, gamma rays, and neutrons, the fluxes generated by the different models display similar spectral shapes, though small systematic differences in magnitude become evident, particularly at lower energies. These differences can be attributed to varying modeling assumptions, including differences in the physical processes and primary particle compositions employed.

The lower panels quantify these differences by displaying the ratios of fluxes predicted by our model to those from the other approaches, thereby offering a clearer view of model-to-model consistency. The ratios remain relatively stable across most energy ranges, indicating a robust level of agreement. However, some deviations are more pronounced in the case of neutrons and gamma rays, particularly at energies below 10 MeV, which can be linked to discrepancies in the treatment of low-energy transport and secondary production. Such deviations are further exacerbated by the fact that our model exclusively considers protons as primary particles, while other studies may include heavier nuclei such as helium or carbon, leading to enhanced production of certain secondaries through nuclear fragmentation and spallation processes. Consequently, while direct comparisons must account for these methodological differences, the consistency between our model and existing frameworks affirms the reliability of our approach in simulating secondary radiation on the Martian surface.

4. Summary and Conclusion

The consideration of zenith angle dependence in the Martian surface radiation environment is crucial for planning future human exploration missions to Mars and for developing a comprehensive global radiation map. Creating such a map requires accounting for multiple factors that influence the radiation dynamics on the Martian surface.

In this study, we employed a Monte Carlo simulation-based approach to calculate the flux of secondary particles reaching the Martian surface, generated by incident primary protons at various zenith angles at the top of the atmosphere. We computed the secondary particle fluence on the Martian surface induced by both SEPs and GCRs.

The SEP-induced results were compared with the ARAMIS model, while the GCR-induced results were validated against measurements from the RAD aboard the Curiosity rover, as well as with previously GEANT4-based established models such as ARAMIS, AtRIS and PLANETOCOSMICS. To enable a consistent comparison, we calculated the total downward flux in our study by integrating the flux of secondary particles reaching the Martian surface over a range of zenith angles. The comparison revealed a generally acceptable level of agreement between our results and those reported in earlier works, thereby validating the reliability of our approach.

In our model, we have concentrated on two crucial factors. First, we investigated the impact of zenith angle on atmospheric column depth. This is of paramount importance because particles reaching the surface from the horizon encounter a greater atmospheric column depth compared to those arriving from the vertical direction. This discrepancy results in changes in the directionality of radiation on the Martian surface. Second, our simulations were conducted under atmospheric conditions specific to surface elevations characteristic of the Gale Crater region—an area of particular scientific interest due to its extensive exploration by the Curiosity rover.

The goal is to elucidate the essential steps required for developing radiation dose maps that accurately incorporate topographic effects. This focused approach enhances our understanding of the radiation environment specific to the target region and contributes valuable insights to the broader context of human exploration planning on Mars.

We derived the flux of downward secondary particles generated through the interaction of primary protons with the Martian atmosphere. These interactions were simulated for different incident zenith angles, each corresponding to a different atmospheric column depth due to the curvature and density profile of the Martian atmosphere. As primary particles enter the atmosphere at varying angles, they experience different path lengths and interaction probabilities, influencing the production and energy distribution of the resulting secondaries. By accounting for these angle-dependent effects, our model enables a more accurate characterization of the radiation environment on the Martian surface across different directions of particle incidence. This directional dependency is critical for understanding surface radiation dose rates, particularly in the context of habitat design and site selection for future crewed missions.

To assess the influence of the Martian atmosphere on radiation transport, we generate matrices that quantify the relationship between incoming primary particles at the top of the atmosphere and the resulting secondary particles detected at the surface. These matrices are parameterized by the zenith angle of atmospheric entry, enabling an angle-dependent analysis of how the atmosphere modulates particle propagation.

Once developed, the matrices can be convolved with any radiation spectra incident at the Martian atmosphere's upper boundary, such as those from GCRs, SEPs, and other potential sources. This method allows for estimation of secondary particle fluxes at the Martian surface across a broad range of entry angles, as long as the particle trajectories intersect the surface. Such a framework provides a flexible and efficient approach for evaluating surface radiation levels under diverse environmental and solar conditions.

Here, we convolved our developed functions with the SEP event of 15 February 2022, as well as GCRs modulated at different levels of solar activity. As a representative case, we present results corresponding to a solar modulation potential of 400 MV.

The convolution of our response functions with SEP spectra reveals notable surface fluxes of low-energy gamma rays, electrons, and neutrons, despite the low intensity of primary protons in that range. This is mainly due to high-energy protons penetrating the atmosphere and initiating spallation reactions, which generate secondary particle cascades. Through this study, we determined the spectra of all secondary particles reaching the Martian surface for the given SEP event across different zenith angles. By extending our analysis across a range of incident angles, we provide a comprehensive characterization of particle fluxes in response to SEP events.

The surface proton flux under GCR conditions shows a dependence on the zenith angle. Vertically incident protons experience minimal attenuation and dominate the flux, especially between 100 MeV and several GeV. At larger angles, increased atmospheric path length leads to stronger energy loss and absorption, significantly reducing low-energy flux. Interestingly, moderate zenith angles can enhance secondary production via nuclear interactions, slightly boosting mid-energy fluxes (100–300 MeV). However, this effect fades at extreme angles due to atmospheric shielding. The spectral peak in the 100–300 MeV range reflects the optimal balance between GCR input and atmospheric interaction efficiency.

Secondary particles produced by primary GCR protons—such as gamma rays, electrons, neutrons, positrons, pions, and deuterons—show varying sensitivity to zenith angle. Unlike primary protons, most secondaries are generated within the atmosphere, resulting in relatively modest angular dependence, especially for gamma rays, electrons, and neutrons. Positrons show slightly stronger angle effects due to their link to gamma-ray cascades. In contrast, positive pions and deuterons exhibit more distinct angular trends and spectral features, with pronounced attenuation at high zenith angles due to their forward-peaked production and greater energy loss.

Our results reveal a pronounced dip in the gamma-ray spectrum between 10 and 100 MeV, which corresponds to the transition between dominant production mechanisms as described by Fujiwara et al. (2025). Nuclear de-excitation and radioactive decay dominate at lower energies, hadronic $\left(\pi^0 \rightarrow \gamma\gamma\right)$ processes prevail at higher energies, and bremsstrahlung contributes weakly in the intermediate range. This agreement confirms the physical interpretation of our observations and demonstrates consistency between our measurements, simulations, and established gamma-ray emission models.

The development of these adaptable matrices holds promise in providing valuable insights into the Martian radiation environment. The resulting data will play a role in constructing topographic maps of Mars in a follow-up study, offering insights into radiation flux variations on the planet. This information allows for assessments of radiation hazards, aiding mission planners in identifying safe areas and natural shelters for astronauts during their exploration and landing on the Martian surface.

Conflict of Interest

The authors declare no conflicts of interest relevant to this study.

Data Availability Statement

The data used in this study are archived in the NASA Planetary Data System's Planetary Plasma Interactions Node at the University of California, Los Angeles. The archival volume includes the full binary raw data files, detailed descriptions of the structures, and higher-level data products in human-readable form. The binary RAD EDR data are archived under (Peterson et al., 2013), while the human-readable RAD RDR data are archived under (Rafkin et al., 2013). The MSL/REMS data archived in the NASA planetary data systems' planetary plasma interactions node (Gomez Elvira, 2013). The data used to produce the figures in the study are available as open access in Zenodo (Khaksari, 2025). More information about the structure of the files is contained within the files themselves.

Acknowledgments

RAD is supported by NASA (HEOMD) under Jet Propulsion Laboratory (JPL) subcontract 1273039 to Southwest Research Institute and in Germany by the German Aerospace Center (DLR) and DLR's Space Administration Grant 50QM1701 to the Christian Albrechts-Universität zu Kiel. JG acknowledges the support by the National Natural Science Foundation of China (Grants 42521007, 42188101). GC's work, bearing the reference EUR CARe N°ANR-18-EURE-0003, has benefited from support managed by the Agence Nationale de la Recherche under the Programme Investissements d'Avenir. PHP and TJS were supported by NASA's Internal Scientist Funding Model (ISFM) Exosphere-Ionosphere-Magnetosphere Modeling (EIMM) team. The work done through the Center for Research and Exploration in Space Science and Technology (CRESST-II) was supported by NASA award number 80GSFC24M0006. Open Access funding enabled and organized by Projekt DEAL.

References

Agostinelli, S., Allison, J., Amako, K., Apostolakis, J., Araujo, H., Arce, P., et al. (2003). GEANT4: A simulation toolkit. *Nuclear Instruments & Methods*, *A506*(3), 250–303. https://doi.org/10.1016/S0168-9002(03)01368-8

Andersson, B., Gustafson, G., & Nilsson-Almqvist, B. (1987). A model for low-pt hadronic reactions with generalizations to hadron-nucleus and nucleus-nucleus collisions. *Nuclear Physics B*, *281*(1–2), 289–309. https://doi.org/10.1016/0550-3213(87)90257-4

Banjac, S., Herbst, K., & Heber, B. (2019). The atmospheric radiation interaction simulator (atris): Description and validation. *Journal of Geophysical Research: Space Physics*, *124*(1), 50–67. https://doi.org/10.1029/2018JA026042

Barcellos-Hoff, M. H., Blakely, E. A., Burma, S. e., Fornace, A. J., Gerson, S., Hlatky, L., et al. (2015). Concepts and challenges in cancer risk prediction for the space radiation environment. *Life Sciences and Space Research*, *6*, 92–103. https://doi.org/10.1016/j.lssr.2015.07.006

Boudard, A., Cugnon, J., David, J.-C., Leray, S., & Mancusi, D. (2013). New potentialities of the liège intranuclear cascade model for reactions induced by nucleons and light charged particles. *Physical Review C*, *87*(1), 014606. https://doi.org/10.1103/PhysRevC.87.014606

Charpentier, G., Ruffenach, M., Benacquista, R., Ecoffet, R., Cappe, A., Dossat, C., et al. (2024). Aramis: A martian radiative environment model built from geant4 simulations. *EDP Sciences*, *14*, 35. https://doi.org/10.1051/swsc/2024032

Cucinotta, F. A., Alp, M., Sulzman, F. M., & Wang, M. (2014). Space radiation risks to the central nervous system. *Life Sciences and Space Research*, *2*, 54–69. https://doi.org/10.1016/j.lssr.2014.06.003

Cucinotta, F. A., & Durante, M. (2006). Cancer risk from exposure to galactic cosmic rays: Implications for space exploration by human beings. *The Lancet Oncology*, *7*(431–436), 682–688. https://doi.org/10.1016/S1470-2045(06)70695-7

Desorgher, L., Flückiger, E. O., & Gurtner, M. (2006). The planetocosmics geant4 application. In *36th cospar scientific assembly* (Vol. 36, p. 2361). Retrieved from https://ui.adsabs.harvard.edu/abs/2006cosp…36.2361D/abstract

Ehresmann, B., Hassler, D., Zeitlin, C., Guo, J., Wimmer-Schweingruber, R., Khaksari, S., & Loeffler, S. (2021). Natural radiation shielding on Mars measured with the MSL/RAD instrument. *Journal of Geophysical Research: Planets*, *126*(8), e2021JE006851. https://doi.org/10.1029/2021JE006851

Fujiwara, T., Owen, E. R., Inoue, Y., Errando, M., Fukuda, K., Nakazawa, K., et al. (2025). The moon as a cosmic-ray spectrometer: Prospects for mev gamma-ray observations. *The Astrophysical Journal*. https://doi.org/10.3847/1538-4357/add68b

Gomez Elvira, J. (2013). MSL rover environmental monitoring station RDR data V1.0, MSL-M-REMS-4-ENVEDR-V1.0. (NASA Planetary Data System). https://doi.org/10.17189/1523028

Gómez-Elvira, J., Armiens, C., Castañer, L., Domínguez, M., Genzer, M., Gómez, F., et al. (2012). REMS: The environmental sensor suite for the Mars Science Laboratory rover. *Space Science Reviews*, *170*(1–4), 583–640. https://doi.org/10.1007/s11214-012-9921-1

Guo, J., Banjac, S., Röstel, L., Terasa, J. C., Herbst, K., Heber, B., & Wimmer-Schweingruber, R. F. (2019). Implementation and validation of the geant4/atris code to model the radiation environment at mars. *Journal of Space Weather and Space Climate*, *9*, A2. https://doi.org/10.1051/swsc/2018051

Guo, J., Khaksarighiri, S., Wimmer-Schweingruber, R. F., Hassler, D. M., Ehresmann, B., Zeitlin, C., et al. (2021). Directionality of the martian surface radiation and derivation of the upward albedo radiation. *Geophysical Research Letters*, *48*(15), e2021GL093912. https://doi.org/10.1029/2021GL093912

Guo, J., Slaba, T. C., Zeitlin, C., Wimmer-Schweingruber, R. F., Badavi, F. F., Böhm, E., et al. (2017). Dependence of the Martian radiation environment on atmospheric depth: Modelling and measurement. *Journal of Geophysical Research: Planetary Science*, *122*(2), 329–341. https://doi.org/10.1002/2016je005206

Guo, J., Wang, B., Whitman, K., Plainaki, C., Zhao, L., Bain, H. M., et al. (2024). Particle radiation environment in the heliosphere: Status, limitations, and recommendations. *Advances in Space Research*. https://doi.org/10.1016/j.asr.2024.03.070

Guo, J., Wimmer-Schweingruber, R. F., Grande, M., Lee-Payne, Z. H., & Matthia, D. (2019). Ready functions for calculating the Martian radiation environment. *Journal of Space Weather and Space Climate*, *9*, A7. https://doi.org/10.1051/swsc/2019004

Guo, J., Zeitlin, C., Wimmer-Schweingruber, R. F., Rafkin, S., Hassler, D. M., Posner, A., et al. (2015). Modeling the variations of dose rate measured by RAD during the first MSL martian year: 2012–2014. *The Astrophysical Journal*, *810*(1), 24. https://doi.org/10.1088/0004-637X/810/1/24

Guo, J., Zeitlin, R. F., Cary, W.-S., Hassler, D. M., Ehresmann, B., Rafkin, S., et al. (2021). Radiation environment for future human exploration on the surface of Mars: The current understanding based on MSL/RAD dose measurements. *Astronomy and Astrophysics Review*, *29*(1), 1–81. https://doi.org/10.1007/s00159-021-00136-5

Hassler, D. M., Zeitlin, C., Wimmer-Schweingruber, R., Böttcher, S., Martin, C., Andrews, J., et al. (2012). The Radiation Assessment Detector (RAD) investigation. *Space Science Reviews*, *170*(1–4), 503–558. https://doi.org/10.1007/s11214-012-9913-1

Jun, I., Garrett, H., Kim, W., Zheng, Y., Fung, S. F., Corti, C., et al. (2024). A review on radiation environment pathways to impacts: Radiation effects, relevant empirical environment models, and future needs. *Advances in Space Research*. https://doi.org/10.1016/j.asr.2024.03.079

Kamiya, K., Ozasa, K., Akiba, S., Niwa, O., Kodama, K., Takamura, N., et al. (2015). Long-term effects of radiation exposure on health. *The lancet*, *386*(9992), 469–478. https://doi.org/10.1016/S0140-6736(15)61167-9

Kennedy, A. R. (2014). Biological effects of space radiation and development of effective countermeasures. *Life Sciences and Space Research*, *1*, 10–43. https://doi.org/10.1016/j.lssr.2014.02.004

Khaksari. (2025). Data for figures plotted in the paper "radiation transport through the martian atmosphere as a function of zenith angle". *Zenodo*. https://doi.org/10.5281/zenodo.17397530

Khaksarighiri, S., Guo, J., Wimmer-Schweingruber, R., & Narici, L. (2021). An easy-to-use function to assess deep space radiation in human brains. *Scientific Reports*, *11*(1), 1–12. https://doi.org/10.1038/s41598-021-90695-5

Khaksarighiri, S., Guo, J., Wimmer-Schweingruber, R. F., Löffler, S., Ehresmann, B., Matthiä, D., et al. (2023). The zenith-angle dependence of the downward radiation dose rate on the martian surface: Modeling versus msl/rad measurement. *Journal of Geophysical Research: Planets*, *128*(4), e2022JE007644. https://doi.org/10.1029/2022JE007644

Khoo, L., Sánchez-Cano, B., Lee, C., Rodríguez-García, L., Kouloumvakos, A., Palmerio, E., et al. (2024). Multispacecraft observations of a widespread solar energetic particle event on 2022 February 15–16. *The Astrophysical Journal*, *963*(2), 107. https://doi.org/10.3847/1538-4357/ad167f

Lobascio, C., Giraudo, M., Bocchini, L., Baiocco, G., Ottolenghi, A., Crisconio, M., & Piccirillo, S. (2018). Perseo: Personal radiation shielding in space, a multifunctional approach. Retrieved from https://ttu-ir.tdl.org/handle/2346/74180

Matthiä, D., & Berger, T. (2017). The radiation environment on the surface of mars–numerical calculations of the galactic component with geant4/planetocosmics. *Life Sciences and Space Research*, *14*, 57–63. https://doi.org/10.1016/j.lssr.2017.03.005

Matthiä, D., Berger, T., Mrigakshi, A. I., & Reitz, G. (2013). A ready-to-use galactic cosmic ray model. *Advances in Space Research*, *51*(3), 329–338. https://doi.org/10.1016/j.asr.2012.09.022

Matthiä, D., Ehresmann, B., Lohf, H., Köhler, J., Zeitlin, C., Appel, J., et al. (2016). The Martian surface radiation environment–a comparison of models and MSL/RAD measurements. *Journal of Space Weather and Space Climate*, *6*(27), 1–17.

Peterson, J., Rafkin, S., Zeitlin, C., Ehresmann, B., Weigle, E., Jeffers, S., & Hassler, D. M. o. (2013). MSL Mars radiation assessment Detector RDR V1.0, MSL-M-RAD-3-RDR-V1.0. (NASA Planetary Data System). https://doi.org/10.17189/1519761

Rafkin, S., Peterson, J., Zeitlin, C., Ehresmann, B., Weigle, E., & Hassler, D. M. o. (2013). MSL Mars radiation assessment Detector EDR V1.0, MSL-M-RAD-2-EDR-V1.0t. (NASA Planetary Data System). https://doi.org/10.17189/1519760

Rafkin, S. C., Zeitlin, C., Ehresmann, B., Hassler, D., Guo, J., Köhler, J., et al. (2014). Diurnal variations of energetic particle radiation at the surface of Mars as observed by the Mars Science Laboratory Radiation Assessment Detector. *Journal of Geophysical Research: Planets*, *119*(6), 1345–1358. https://doi.org/10.1002/2013je004525

Rose, P. (1991). *Endf-201: Endf/b-vi summary documentation (Tech. Rep.)*. Brookhaven National Lab.(BNL), Upton, NY (United States). https://doi.org/10.2172/5733676

Simpson, J. (1983). Elemental and isotopic composition of the galactic cosmic rays. *Annual Review of Nuclear and Particle Science*, *33*(1), 323–382. https://doi.org/10.1146/annurev.ns.33.120183.001543

Wilson, J., Clowdsley, M., Cucinotta, F., Tripathi, R., Nealy, J., & De Angelis, G. (2004). Deep space environments for human exploration. *Advances in Space Research*, *34*(6), 1281–1287. https://doi.org/10.1016/j.asr.2003.10.052

Wimmer-Schweingruber, R. F., Köhler, J., Hassler, D. M., Guo, J., Appel, J.-K., Zeitlin, C., et al. (2015). On determining the zenith angle dependence of the Martian radiation environment at gale crater altitudes. *Geophysical Research Letters*, *42*(24), 10–557. https://doi.org/10.1002/2015GL066664

Zhang, J., Guo, J., Zhang, Y., Cao, Y., Dobynde, M. I., Li, C., et al. (2024). The 2022 February 15 solar energetic particle event at mars: A synergistic study combining multiple radiation detectors on the surface and in orbit of mars with models. *Geophysical Research Letters*, *51*(19), e2024GL111775. https://doi.org/10.1029/2024GL111775